




Cite this: *New J. Chem.*, 2022, 46, 13082

Enhanced catalytic activity of perovskite $\text{La}_{1-x}\text{Sr}_x\text{MnO}_{3+\delta}$ for the oxygen reduction reaction†

Wencong Wang, Wei Liu,  Masao Kamiko and Shunsuke Yagi *

Fuel cells are considered promising next-generation energy conversion devices because of their high efficiency and environment-friendly attributes. However, a large overpotential for the oxygen reduction reaction (ORR) at the cathode minimizes the energy efficiency of these devices. In this context, ORR catalysts based on 3d transition metal oxides have attracted significant attention as affordable and highly active catalysts with potential to replace expensive noble metal catalysts (e.g., Pt). In this study, the ORR catalytic activities of ‘oxygen-excess’ perovskite $\text{La}_{1-x}\text{Sr}_x\text{MnO}_{3+\delta}$ ($x = 0, 0.1, 0.2, 0.3$, and 0.4), with both higher activity and stability compared to a regular perovskite, i.e., $\text{La}_{0.8}\text{Sr}_{0.2}\text{MnO}_3$, were investigated and the performances were evaluated with respect to changes in the Mn valence number, amount of cation vacancies and Mn–O bond length. Sr substitution can affect the formation of Mn^{4+} ions and modulate the cation vacancies, thus changing the length of the Mn–O bond. The lowest overpotential was observed for $\text{La}_{0.8}\text{Sr}_{0.2}\text{MnO}_{3+\delta}$, where the Mn–O bond length was the shortest, resulting in the highest activity. Overall, this work provides guidelines to improve the ORR catalytic activity of Mn-based perovskites.

Received 26th May 2022,
Accepted 9th June 2022

DOI: 10.1039/d2nj02619h

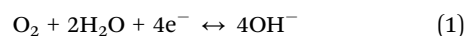
rsc.li/njc

1. Introduction

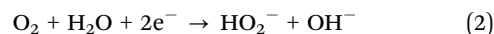
The rapidly increasing global environmental pollution caused by the massive use of fossil fuels necessitates the development and use of clean and renewable energy resources.^{1,2} Accordingly, various energy storage and conversion devices have been proposed in the last few decades.^{3–7} Among them, fuel cells have attracted considerable attention as next-generation clean energy conversion devices because of their high energy conversion efficiency (60–70%) and environment-friendly attributes.⁸ In fuel cells, the chemical energy stored in fuels, such as hydrogen, methanol, and ethanol, is directly converted into electrical energy at the anode, while a simultaneous oxygen reduction reaction (ORR) occurs at the cathode. Both the fuel oxidation reaction and ORR must be carried out in the presence of a catalyst that significantly lowers the overpotential, leading to an efficient energy conversion.^{9,10} However, ORR catalysts must be carefully designed as the ORR is a kinetically slow process,^{11,12} thus, catalysts that exhibit both high activity and stability are generally expensive, and those with good attributes yet low costs are yet to be found.

For the ORR in alkaline solutions, two pathways are possible as shown below.¹³

4-Electron pathway (eqn (1)):



2-Electron pathway (eqn (2)):



Noble metals, such as Pt and Pd, have been widely used as ORR catalysts with excellent catalytic activity.^{14,15} However, these are expensive and constrained by limited resources. Alternative catalysts, which are abundant and thus cheap yet similarly effective to or more effective than the precious metals in catalyzing the ORR, can solve the cost issue associated with ORR catalysts.^{16,17} Transition metal oxides are considered as the most promising alternative catalysts.^{18,19} In particular, perovskites with a general formula of ABO_3 are of great interest because of their high catalytic activity, significantly low cost, and compositional flexibility.^{20,21} Hyodo *et al.* reported the effects of A- and B-site cations on the ORR catalytic activity using various types of perovskites.²² For the A-site cations, La-based perovskites showed a higher ORR catalytic activity than Pr-, Nd-, and Sm-based perovskites. Regarding the B-site cations, Mn, Fe, Co, and Ni with partially filled 3d orbitals showed high ORR catalytic activities. Therefore, LaMnO_3 has

Institute of Industrial Science, The University of Tokyo, 4-6-1 Komaba, Meguro-ku, Tokyo, 153-8505, Japan. E-mail: syagi@iis.u-tokyo.ac.jp

† Electronic supplementary information (ESI) available. See DOI: <https://doi.org/10.1039/d2nj02619h>



attracted considerable attention as an ORR catalyst. Notably, the perovskite structure allows the formation of non-stoichiometric compounds, such as oxygen-deficient $\text{LaMnO}_{3-\delta}$ and 'oxygen-excess' $\text{LaMnO}_{3+\delta}$. It is worth noting that 'oxygen-excess' does not mean the existence of interstitial oxygen ions. Roosmalen *et al.* proposed that the 'oxygen-excess' originates from the existence of cation vacancies at La and Mn sites, and the amounts of La and Mn vacancies should be equal.²³ The real chemical formula of $\text{LaMnO}_{3+\delta}$ should be $\text{La}_{1-\gamma}\text{MnO}_{1-\gamma}\text{O}_3$ ($\gamma = \delta/(3 + \delta)$), but for simplicity the former expression is used as the name of the sample. Elemental substitution is a method frequently used to modulate the defect density and electronic structure of LaMnO_3 to improve its ORR catalytic activity.^{24,25} Commonly used elements for replacing La at the A-site are alkaline earth metals, such as Ca and Sr, and those for replacing Mn at the B-site are 3d transition metals, such as Ni, Fe, and Co. Furthermore, the partial replacement of La with Sr has been proven effective in improving the ORR catalytic activity *via* modulation of the Mn valence state and O vacancy concentration.^{26,27} Most current studies on LaMnO_3 have been concerned with either stoichiometric LaMnO_3 or oxygen-deficient $\text{LaMnO}_{3-\delta}$; however, the exploration of 'oxygen-excess' $\text{LaMnO}_{3+\delta}$ and its electronic structure modulation induced by Sr replacement is scarce.

In this study, we investigated the effects of Sr substitution in nonstoichiometric $\text{LaMnO}_{3+\delta}$ on the ORR catalytic activity in an oxygen-saturated 0.1 M KOH aqueous solution. We found that the Sr-substituted and 'oxygen-excess' $\text{La}_{1-x}\text{Sr}_x\text{MnO}_{3+\delta}$ compounds ($x = 0, 0.1, 0.2, 0.3$, and 0.4) showed higher catalytic activity and stability than the normal Sr-substituted perovskite (*i.e.*, $\text{La}_{0.8}\text{Sr}_{0.2}\text{MnO}_3$). Through a combination of spectroscopic and electrochemical studies, we specifically examined the intrinsic reasons for the ORR catalytic activity difference of the $\text{La}_{1-x}\text{Sr}_x\text{MnO}_{3+\delta}$ series. The catalytic activity dependence on the Mn valence state, cation vacancies and Mn–O bond length is discussed.

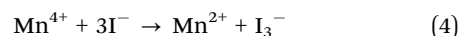
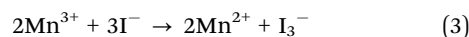
2. Experimental

2.1. Synthesis of $\text{La}_{1-x}\text{Sr}_x\text{MnO}_{3+\delta}$

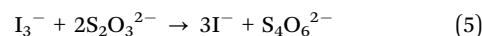
The $\text{La}_{1-x}\text{Sr}_x\text{MnO}_{3+\delta}$ ($x = 0, 0.1, 0.2, 0.3$, and 0.4) compounds were synthesized by a sol-gel process. First, $\text{La}(\text{NO}_3)_3 \cdot 6\text{H}_2\text{O}$ (Nacalai Tesque, Inc. 99.9%), $\text{Sr}(\text{NO}_3)_2$ (Sigma-Aldrich, 99.0%), and $\text{Mn}(\text{NO}_3)_2 \cdot 6\text{H}_2\text{O}$ (Nacalai Tesque, Inc. 98.0%) were weighed according to their stoichiometric ratios and dissolved in 30 mL deionized water. After stirring the solutions for 2 h, 4.61 g of citric acid (Nacalai Tesque, Inc., 99.5%) was added to each solution, which were then stirred for another 2 h. Subsequently, the solutions were heated to 80 °C and maintained at that temperature for 12 h to obtain yellow gel precursors. The final products were obtained after the calcination of the gel precursors at 750 °C for 5 h. For comparison, stoichiometric $\text{La}_{0.8}\text{Sr}_{0.2}\text{MnO}_3$ (99%) powder was bought from Sigma-Aldrich.

2.2. Characterization

The crystal structure was examined by XRD measurements (Ultima IV, Rigaku Co., Ltd) of the powder samples using a molybdenum X-ray tube ($\lambda = 0.7107 \text{ \AA}$). Morphologies were observed by scanning electron microscopy (SEM, JEOL JSM-6010 LA) and high-resolution transmission electron microscopy (HRTEM, JEOL JEM-2100). The valence state of Mn was analyzed by XPS using a ULVAC-PHI Quantera instrument. ICP-AES was conducted to determine the ratios of La, Sr, and Mn using a sample dissolved in a 1 M HCl aqueous solution. The sum of $2[\text{Mn}^{3+}]$ and $[\text{Mn}^{4+}]$ was determined by iodometry using a titration device (COM-A19S, Hiranuma Co., Ltd). In detail, 10 mg of the sample was mixed with 40 mL of 0.1 g mL^{-1} KI solution. Then, 3 mL of 6 mol L^{-1} HCl was added to dissolve the sample. All the Mn^{3+} and Mn^{4+} ions will be reduced to Mn^{2+} by I^- as shown below:²⁸



Then titration was performed using 10 mmol L^{-1} $\text{Na}_2\text{S}_2\text{O}_3$ solution assuming the following reaction:



The numbers of La^{3+} , Sr^{2+} , Mn^{3+} , Mn^{4+} , La and Mn vacancies ($V_{\text{A-site}}$ and $V_{\text{B-site}}$) were estimated by considering the results of ICP, iodometry, and charge balance. XAS was performed in the transmission mode to obtain Mn K-edge absorption spectra at SPring-8 in Japan with a Si(111) double-crystal monochromator operated at 8 GeV. The Athena program was used for the background subtraction and normalization of the XAS data, and the Artemis program integrated with the IFEFFIT package was used for shell fitting of the XAS spectra in the *R* space.²⁹

2.3. Electrochemical measurements

The catalyst ink used for testing was prepared as follows. First, 10 mL of Nafion solution (5 mass% in a mixture of lower aliphatic alcohols and water, 45% water, Sigma-Aldrich) and 20 mL of 0.1 M KOH aqueous solution were mixed to obtain a K^+ -exchanged Nafion solution. Then, 0.3 mL of the K^+ -exchanged Nafion solution, 50 mg of the perovskite catalyst, and 10 mg of acetylene black were mixed in a 10 mL volumetric flask, and the flask was filled to 10 mL with a 6 : 4 (v/v) mixture of water and ethanol.

Electrochemical measurements were conducted using a three-electrode cell with a rotating ring disk electrode (RRDE) system (RRDE-3A, BAS Inc.) at a speed of 1600 rotations per min in 0.1 M KOH aqueous solution. The RRDE consisted of a glassy carbon disk (area $\sim 0.126 \text{ cm}^2$) and a platinum ring (area $\sim 0.188 \text{ cm}^2$). A Pt wire was used as the counter electrode, and a Hg/HgO (0.1 M KOH aqueous solution) electrode was used as the reference electrode.

Before the electrochemical measurements, oxygen was purged into the electrolyte solution for 20 min to obtain an oxygen-saturated solution. Note that, although oxygen bubbling



was stopped after achieving the saturation in the solution, the oxygen flow was maintained above the solution during the measurements. LSV was performed at a scan rate of 10 mV s^{-1} in the potential range from 0.3 to $-0.6 \text{ V vs. Hg/HgO}$ (0.1 M aq. KOH). The potential of the ring electrode was set to 0.4 V vs. Hg/HgO to oxidize HO_2^- formed on the disk electrode.

The production fraction of HO_2^- and electron transfer number (n) were calculated using the following equations:

$$\text{HO}_2^-(\%) = 200 \frac{I_r}{I_r + I_d} \quad (6)$$

$$n = 4 \frac{I_d}{I_r + I_d} \quad (7)$$

where I_d is the disk current, I_r is the ring current, and $N (= 0.424)$ is the capture rate of the RRDE electrode in this study.

All the potential values measured vs. Hg/HgO (0.1 M aq. KOH), *i.e.*, E (V vs. Hg/HgO), were converted to the potential values vs. reversible hydrogen electrode, E (V vs. RHE), using the following relationship:

$$E (\text{V vs. RHE}) = E (\text{V vs. Hg/HgO}) + 0.926 \quad (8)$$

3. Results and discussion

3.1 Structure, morphology, and composition

The crystal structures of the prepared $\text{La}_{1-x}\text{Sr}_x\text{MnO}_{3+\delta}$ compounds were analyzed by X-ray diffraction (XRD) (Fig. 1a). The

diffraction peaks for all samples with different amounts of Sr matched well with those for the reported perovskite-type structure of LaMnO_3 (ICSD#75070).³⁰ The lattice parameters obtained from the XRD patterns are listed in Table S1 (ESI†). The crystal system is rhombohedral and the space group is $R\bar{3}c$, which has been reported to have a higher ORR catalytic activity than the orthorhombic structure.³¹ In Fig. 1b–f, the d -spacing obtained from the high-resolution TEM images also confirmed the rhombohedral structure of these samples. In the XRD profile of $\text{La}_{0.6}\text{Sr}_{0.4}\text{MnO}_{3+\delta}$, minor impurity peaks appeared at approximately 12° , which corresponds to SrCO_3 (ICSD#15195), possibly formed by a reaction of Sr with citric acid during synthesis. Highly pure samples could not be obtained above $x = 0.6$, as shown in Fig. S1 (ESI†). SEM images and TEM images in Fig. S2 and S3 (ESI†) suggest that all the samples have similar morphologies. The primary particle diameters of all the samples are mostly in the range of 10–20 nm as shown in Fig. S3 (ESI†), indicating that Sr-substitution does not change the morphology and particle size obviously.

Inductively coupled plasma atomic emission spectroscopy (ICP-AES) and iodometry were performed to determine the numbers of La, Sr, and Mn (Mn^{3+} and Mn^{4+}) assuming a chemical formula of $\text{La}_{1-x-y}(\text{V}_{\text{A-site}})_y\text{Sr}_x\text{Mn}_{1-x-y}^{3+}\text{Mn}_y^{4+}(\text{V}_{\text{B-site}})_y\text{O}_3$,²³ as shown in Table 1. The amount of cation vacancies is decreased, while the fraction of Mn^{4+} monotonically increased from 0.341 to 0.680 to maintain electrical neutrality as the amount of Sr is increased from 0 to 0.4.

3.2 Energy spectroscopies

X-Ray photoelectron spectroscopy (XPS) was conducted to analyze the chemical environment of Mn and O. As can be seen from the Mn 2p XPS profiles in Fig. 2a, Mn $2p_{3/2}$ and Mn $2p_{1/2}$ peaks are centered at 641.5 and 653.3 eV, respectively. The spin-orbit splitting value (ΔE) between Mn $2p_{3/2}$ and Mn $2p_{1/2}$ is 11.8 eV. Through XPS fitting, both the Mn $2p_{1/2}$ and $2p_{3/2}$ peaks can be deconvoluted into three peaks, comprising a primary and a satellite peak for Mn^{3+} and a peak for Mn^{4+} .^{32,33} The obtained binding energies are listed in Table S2 (ESI†). In all the samples, Mn exists in both +3 and +4 valence states, while the valence number of Mn can be considered +3 in the completely stoichiometric LaMnO_3 . The atomic ratios of Mn^{3+} and Mn^{4+} obtained *via* XPS fitting are listed in Table 2. The percentage of Mn^{4+} increased from 32.3% to 67.4%, which is in good agreement with the titration results shown in Table 1. O 1s XPS profiles are shown in Fig. 2b, which can be assigned to two peaks: a low binding energy peak, which represents the lattice oxygen O_L , and a high energy peak, which can be attributed to the surface adsorbed oxygen species O_s .^{34,35} The $\text{La}_{0.8}\text{Sr}_{0.2}\text{MnO}_{3+\delta}$ sample shows the highest surface adsorbed oxygen species concentration as shown in Table 2. This may partially contribute to ORR catalytic activity.

X-Ray absorption spectroscopy (XAS) is a powerful tool to analyze the oxidation states and bond conditions. Fig. 3a presents the X-ray absorption near-edge spectra (XANES, Mn K-edge) of the $\text{La}_{1-x}\text{Sr}_x\text{MnO}_{3+\delta}$ samples. The spectra of all the samples are located between the spectra of standard Mn_2O_3

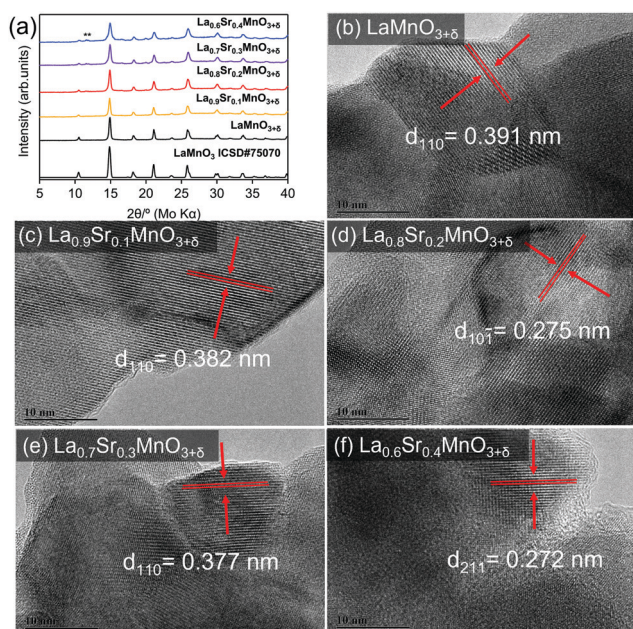
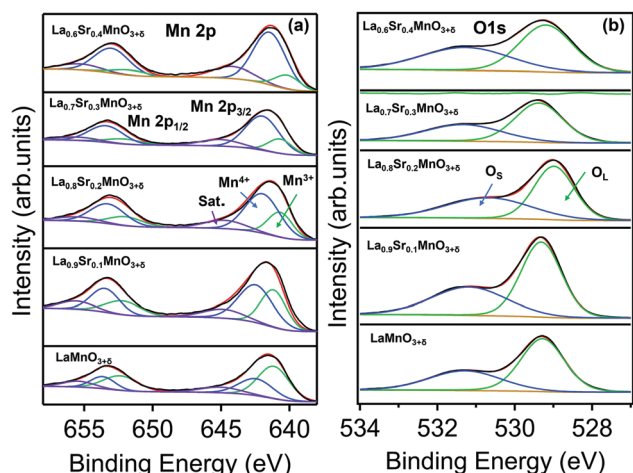


Fig. 1 (a) XRD patterns measured with Mo $K\alpha$ radiation (wavelength: 0.7107 Å). The peak at 12° (marked with **) corresponds to an impurity peak of SrCO_3 . (b–f) High-resolution TEM images with lattice spacings.



Table 1 Actual composition analysis using the chemical formula of $\text{La}_{1-x-y}(\text{V}_{\text{A-site}})_y\text{Sr}_x\text{Mn}_a^{3+}\text{Mn}_b^{4+}(\text{V}_{\text{B-site}})_y\text{O}_3$

Sample name	La	Sr	$\text{V}_{\text{A-site}}$	Mn^{3+}	Mn^{4+}	$\text{V}_{\text{B-site}}$
$\text{LaMnO}_{3+\delta}$	0.943 ± 0.002	0	0.057 ± 0.012	0.602 ± 0.012	0.341 ± 0.012	0.057 ± 0.012
$\text{La}_{0.9}\text{Sr}_{0.1}\text{MnO}_{3+\delta}$	0.856 ± 0.001	0.094 ± 0.001	0.050 ± 0.014	0.553 ± 0.014	0.397 ± 0.014	0.050 ± 0.014
$\text{La}_{0.8}\text{Sr}_{0.2}\text{MnO}_{3+\delta}$	0.749 ± 0.002	0.203 ± 0.002	0.048 ± 0.011	0.457 ± 0.011	0.494 ± 0.011	0.048 ± 0.011
$\text{La}_{0.7}\text{Sr}_{0.3}\text{MnO}_{3+\delta}$	0.640 ± 0.002	0.315 ± 0.002	0.045 ± 0.015	0.369 ± 0.015	0.586 ± 0.015	0.045 ± 0.015
$\text{La}_{0.6}\text{Sr}_{0.4}\text{MnO}_{3+\delta}$	0.545 ± 0.001	0.410 ± 0.001	0.044 ± 0.012	0.275 ± 0.012	0.680 ± 0.012	0.044 ± 0.012

**Fig. 2** (a) XPS Mn 2p spectra and (b) XPS O 1s spectra of $\text{La}_{1-x}\text{Sr}_x\text{MnO}_{3+\delta}$.**Table 2** Atomic concentration ratios of Mn^{3+} and Mn^{4+} ; O_S and O_L estimated by fitting the XPS profiles shown in Fig. 2

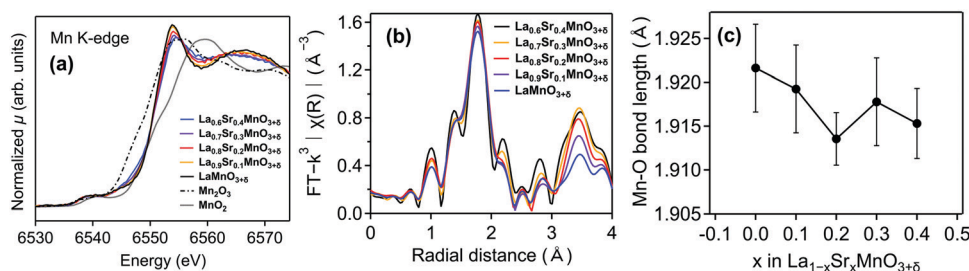
Sample	Mn^{3+} (%)	Mn^{4+} (%)	O_S (%)	O_L (%)
$\text{LaMnO}_{3+\delta}$	67.8	32.3	37.8	62.2
$\text{La}_{0.9}\text{Sr}_{0.1}\text{MnO}_{3+\delta}$	49.4	50.6	40.3	59.7
$\text{La}_{0.8}\text{Sr}_{0.2}\text{MnO}_{3+\delta}$	41.1	58.9	45.5	54.5
$\text{La}_{0.7}\text{Sr}_{0.3}\text{MnO}_{3+\delta}$	34.7	65.3	37.4	62.6
$\text{La}_{0.6}\text{Sr}_{0.4}\text{MnO}_{3+\delta}$	32.6	67.4	44.1	55.9

and MnO_2 , which again indicates that the valence states of Mn in all these samples are between +3 and +4, consistent with the XPS and ICP/iodometry analyses. Fig. 3b shows the extended X-ray absorption fine structure (EXAFS) spectra of the Mn K-edge in the R space. The first peak between 1.0 and 2.0 Å is related to the Mn–O bond.^{36,37} To evaluate the Mn–O bond

length, EXAFS fitting was performed by assuming a rhombohedral LaMnO_3 structure with the first nearest shell model using the Artemis program integrated with the IFEFFIT package in the 1.0–2.0 Å range.²⁹ The Mn–O bond lengths, determined from the fitting (*cf.* Table S3, ESI†), are shown in Fig. 3c. When x was increased from 0 to 0.2, the Mn–O bond length gradually decreased and reached a minimum at $x = 0.2$. The shortest bond length may be a result of the combination of an increase in the oxidation state of Mn and a decrease in Mn vacancies as shown in Tables 1 and 2. In addition, the shortest Mn–O bond length of the $\text{La}_{0.8}\text{Sr}_{0.2}\text{MnO}_{3+\delta}$ sample may result in the strongest interaction between Mn and O, which can explain the highest surface adsorbed oxygen species concentration obtained from O 1s XPS spectral fitting results.

3.3 ORR catalytic properties

The ORR catalytic activity of $\text{La}_{1-x}\text{Sr}_x\text{MnO}_{3+\delta}$ ($x = 0, 0.1, 0.2, 0.3$, and 0.4) was evaluated using a rotating ring disk electrode (RRDE) system in a 0.1 M KOH aqueous solution (Fig. 4). A comparison of the linear sweep voltammograms (LSVs) in Fig. 4a suggests that $\text{La}_{0.8}\text{Sr}_{0.2}\text{MnO}_{3+\delta}$ exhibits the highest current density among all perovskites in the $\text{La}_{1-x}\text{Sr}_x\text{MnO}_{3+\delta}$ series. The current density is not linearly correlated with the value of x , and it decreases in the following order: $x = 0.2 > x = 0.4 > x = 0.3 > x = 0.1 > x = 0$. The overpotentials (E_{over}) determined at -2 mA cm^{-2} and the onset potentials (E_{onset}) determined at -0.1 mA cm^{-2} obtained from the LSVs are listed in Table 3. E_{over} , E_{onset} , and the current density are all correlated; a lower E_{over} corresponds to a higher current density. Therefore, $\text{La}_{0.8}\text{Sr}_{0.2}\text{MnO}_{3+\delta}$ exhibited both the lowest E_{over} and the highest current density, indicating the highest catalytic activity among others with different Sr substitution. In the ORR, the 4-electron pathway is preferred over the 2-electron pathway because of the higher energy conversion efficiency of

**Fig. 3** (a) Normalized Mn K-edge XANES profiles of $\text{La}_{1-x}\text{Sr}_x\text{MnO}_{3+\delta}$, Mn_2O_3 and MnO_2 . (b) Fourier transform of the Mn K-edge EXAFS spectra of $\text{La}_{1-x}\text{Sr}_x\text{MnO}_{3+\delta}$ in the R space. (c) Fitted Mn–O bond length in $\text{La}_{1-x}\text{Sr}_x\text{MnO}_{3+\delta}$. Error bars show the standard deviations.

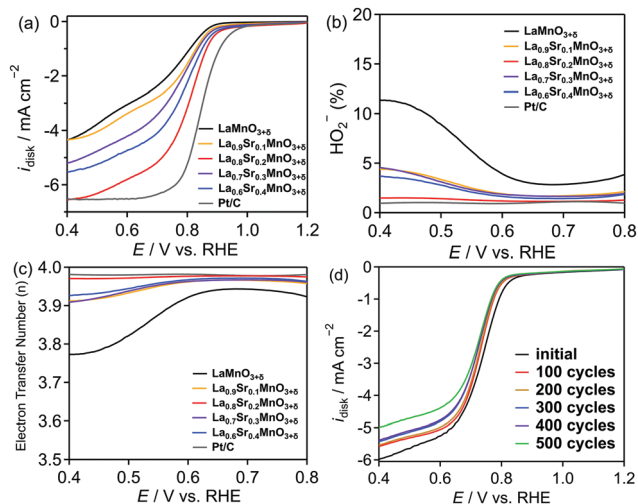


Fig. 4 (a) LSV curves obtained from the measurements in 0.1 M KOH aqueous solution using the disk electrode modified with different catalysts with a scan rate of 10 mV s^{-1} at 1600 rpm. Pt/C served as the reference catalyst. (b) Fraction of HO_2^- , (c) electron transfer number (n), and (d) LSV curves measured using $\text{La}_{0.8}\text{Sr}_{0.2}\text{MnO}_{3+\delta}$ during 500 cycles of cyclic voltammetry.

Table 3 Overpotential and onset potential at current densities of -2 and -0.1 mA cm^{-2} , respectively, obtained from the LSV curves of the ORR using $\text{La}_{1-x}\text{Sr}_x\text{MnO}_{3+\delta}$ and Pt/C as catalysts

Sample	E_{over} (V)	E_{onset} (V vs. RHE)
$\text{LaMnO}_{3+\delta}$	0.494	0.900
$\text{La}_{0.9}\text{Sr}_{0.1}\text{MnO}_{3+\delta}$	0.456	0.961
$\text{La}_{0.8}\text{Sr}_{0.2}\text{MnO}_{3+\delta}$	0.398	1.135
$\text{La}_{0.7}\text{Sr}_{0.3}\text{MnO}_{3+\delta}$	0.444	1.035
$\text{La}_{0.6}\text{Sr}_{0.4}\text{MnO}_{3+\delta}$	0.421	1.069
Pt/C	0.355	1.085

the former pathway. The production fraction of HO_2^- ($\text{HO}_2^-\%$) and electron transfer number (n)³⁸ were calculated using eqn (6) and (7) (see the Experimental section for details) using the disk and ring currents (Fig. S4, ESI†), as shown in Fig. 4b and c, respectively. $\text{LaMnO}_{3+\delta}$ produces $>10\%$ HO_2^- at 0.4 V vs. RHE through the 2-electron pathway, resulting in the lowest value of n (3.78) in the series. With 10% Sr substitution (*i.e.*, $\text{La}_{0.9}\text{Sr}_{0.1}\text{MnO}_{3+\delta}$), the $\text{HO}_2^-\%$ decreases significantly to $<5\%$, and n is close to 4. In particular, the $\text{HO}_2^-\%$ and n for $\text{La}_{0.8}\text{Sr}_{0.2}\text{MnO}_{3+\delta}$ are very close to those of Pt, indicating the excellent 4-electron selectivity of the catalyst. As shown in Fig. 3c and Table 3, the trends for the changes in overpotential and Mn–O bond length are fully consistent. The above trends are in agreement with the report by Suntivich *et al.*³¹ who stated that the ORR catalytic activity is related to the B–O covalency in the ABO_3 perovskite, where a strong covalency of the B–O bond can increase the driving force of the rate-limiting $\text{O}^{2-}/\text{OH}^-$ exchange reaction occurring on the surface B ions. According to the EXAFS fitting results, the $\text{La}_{0.8}\text{Sr}_{0.2}\text{MnO}_{3+\delta}$ sample had the shortest Mn–O bond length with a high degree of covalency, resulting in the highest ORR catalytic activity in the series.

Durability of the catalysts is another important aspect for ORR catalysis. The LSV curves for the best sample, $\text{La}_{0.8}\text{Sr}_{0.2}\text{MnO}_{3+\delta}$, measured during 500 cycles of cyclic voltammetry, are shown in Fig. 4d. For comparison, the LSV curves for $\text{La}_{0.8}\text{Sr}_{0.2}\text{MnO}_3$ over 500 cycles are shown in Fig. S5 (ESI†). After 500 cycles, the current density for $\text{La}_{0.8}\text{Sr}_{0.2}\text{MnO}_3$ was significantly lower than the initial value, indicating poor stability. In contrast, for the cycling using $\text{La}_{0.8}\text{Sr}_{0.2}\text{MnO}_{3+\delta}$, the decrease and increase in the current density and overpotential, respectively, were smaller and gradual. Even after 500 cycles, the overpotential at -2 mA cm^{-2} increased only by 5.5% compared to the initial value, indicating excellent stability. In addition, the Mn 2p XPS profiles for $\text{La}_{0.8}\text{Sr}_{0.2}\text{MnO}_{3+\delta}$ before and after 500 cycles of cyclic voltammetry are shown in Fig. S6 (ESI†), and the atomic ratios of Mn^{3+} and Mn^{4+} estimated using the XPS profiles are listed in Table S4 (ESI†). After 500 cycles, the ratio of Mn^{4+} was decreased, suggesting a gradual reduction of Mn^{4+} to Mn^{3+} during 500 cycles. Thus, the slight increase of the overpotential for the ORR of $\text{La}_{0.8}\text{Sr}_{0.2}\text{MnO}_{3+\delta}$ of about 5.5% after 500 cycles as shown in Fig. 4d could have been caused by the decrease in the Mn valence number.

4. Conclusions

In this study, we synthesized a series of perovskites with a general formula of $\text{La}_{1-x}\text{Sr}_x\text{MnO}_{3+\delta}$ ($x = 0, 0.1, 0.2, 0.3$, and 0.4) via Sr substitution of ‘oxygen-excess’ $\text{LaMnO}_{3+\delta}$ and investigated the effect of Sr substitution on the ORR catalytic activity of the resultant catalysts. Sr substitution leads to an increase in the Mn valence state and a decrease in the amount of cation vacancies, which were verified by iodometry and XPS. The opposite trends in the valence state of Mn and the amount of Mn vacancies may have led to a minimum in the Mn–O bond length. The ORR catalytic activity was found to be correlated with the Mn–O bond length; the shortest Mn–O bond length (and the highest covalency) of $\text{La}_{0.8}\text{Sr}_{0.2}\text{MnO}_{3+\delta}$ among others in the series was responsible for the highest ORR catalytic activity of this catalyst. The high catalytic activity, high 4-electron selectivity close to Pt and the excellent stability make this material a promising ORR catalyst that can replace precious metals.

Author contributions

Wencong Wang: experiment, analysis, and writing. Wei Liu: XAFS analysis. Masao Kamiko: XPS experimental support. Shunsuke Yagi: supervision, writing, reviewing, and editing.

Funding sources

This research was financially supported by a Grant-in-Aid for the University of Tokyo Excellent Young Researcher and Grant-in-Aid for Scientific Research (20H05180, 22H04497) commissioned by the Japan Society for the Promotion of Science. X-Ray absorption spectroscopy (XAS) data were obtained at the



BL14B2 beamline (Proposal No. 2021B1902) of SPring-8 with support from the Japan Synchrotron Radiation Research Institute.

Conflicts of interest

The authors declare that they have no known competing financial interests or personal relationships that influenced the work reported in this study.

Acknowledgements

We thank Prof. Toru H. Okabe and Dr Takanari Ouchi for their support with the ICP-AES measurements. We also thank Prof. Ikuya Yamada and Dr Yuichi Okazaki for giving an opportunity to measure the XAS data.

References

- 1 C. Tarhan and M. A. Çil, A study on hydrogen, the clean energy of the future: Hydrogen storage methods, *J. Energy Storage*, 2021, **40**, 102676.
- 2 C. Liao, J. T. Erbaugh, A. C. Kelly and A. Agrawal, Clean energy transitions and human well-being outcomes in Lower and Middle Income Countries: A systematic review, *Renew. Sustainable Energy Rev.*, 2021, **145**, 111063.
- 3 L. Ye and X. Li, A dynamic stability design strategy for lithium metal solid state batteries, *Nature*, 2021, **593**, 218–222.
- 4 M. Singh, D. Zappa and E. Comini, Solid oxide fuel cell: Decade of progress, future perspectives and challenges, *Int. J. Hydrogen Energy*, 2021, **46**, 27643–27674.
- 5 J. Han, S. Yagi, H. Takeuchi, M. Nakayama and T. Ichitsubo, Catalytic mechanism of spinel oxides for oxidative electrolyte decomposition in Mg rechargeable batteries, *J. Mater. Chem. A*, 2021, **9**, 26401–26409.
- 6 M. Wang, J. Han, W. Liu, M. Kamiko and S. Yagi, Energy storage mechanism of monocrystalline layered FePS₃ and FePSe₃ as active materials for Mg batteries and pseudocapacitors, *J. Alloys Compd.*, 2021, **883**, 160822.
- 7 M. Zhi, C. Xiang, J. Li, M. Li and N. Wu, Nanostructured carbon-metal oxide composite electrodes for supercapacitors: A review, *Nanoscale*, 2013, **5**, 72–88.
- 8 M. Secanell, J. Wishart and P. Dobson, Computational design and optimization of fuel cells and fuel cell systems: A review, *J. Power Sources*, 2011, **196**, 3690–3704.
- 9 F. Yang, X. Bao, Y. Zhao, X. Wang, G. Cheng and W. Luo, Enhanced HOR catalytic activity of PGM-free catalysts in alkaline media: The electronic effect induced by different heteroatom doped carbon supports, *J. Mater. Chem. A*, 2019, **7**, 10936–10941.
- 10 Y. J. Wang, W. Long, L. Wang, R. Yuan, A. Ignaszak, B. Fang and D. P. Wilkinson, Unlocking the door to highly active ORR catalysts for PEMFC applications: Polyhedron-engineered Pt-based nanocrystals, *Energy Environ. Sci.*, 2018, **11**, 258–275.
- 11 C. Lo Vecchio, A. Serov, H. Romero, A. Lubers, B. Zulevi, A. S. Aricò and V. Baglio, Commercial platinum group metal-free cathodic electrocatalysts for highly performed direct methanol fuel cell applications, *J. Power Sources*, 2019, **437**, 226948.
- 12 Y. Shao, J. P. Dodelet, G. Wu and P. Zelenay, PGM-Free Cathode Catalysts for PEM Fuel Cells: A Mini-Review on Stability Challenges, *Adv. Mater.*, 2019, **31**, 1–8.
- 13 X. Ge, A. Sumboja, D. Wu, T. An, B. Li, F. W. T. Goh, T. S. A. Hor, Y. Zong and Z. Liu, Oxygen Reduction in Alkaline Media: From Mechanisms to Recent Advances of Catalysts, *ACS Catal.*, 2015, **5**, 4643–4667.
- 14 M. Liu, Z. Zhao, X. Duan and Y. Huang, Nanoscale Structure Design for High-Performance Pt-Based ORR Catalysts, *Adv. Mater.*, 2019, **31**, 1–8.
- 15 L. E. Betancourt, A. Rojas-Pérez, I. Orozco, A. I. Frenkel, Y. Li, K. Sasaki, S. D. Senanayake and C. R. Cabrera, Enhancing ORR Performance of Bimetallic PdAg Electrocatalysts by Designing Interactions between Pd and Ag, *ACS Appl. Energy Mater.*, 2020, **3**, 2342–2349.
- 16 L. Du, L. Xing, G. Zhang, M. Dubois and S. Sun, Strategies for Engineering High-Performance PGM-Free Catalysts toward Oxygen Reduction and Evolution Reactions, *Small Methods*, 2020, **4**, 1–28.
- 17 E. F. Holby, Improving platinum group metal-free oxygen reduction reaction electrocatalyst activity: suggestions from density functional theory studies, *Curr. Opin. Electrochem.*, 2021, **25**, 100631.
- 18 J. Wang, Z. Zhang, J. Ding, C. Zhong, Y. Deng, X. Han and W. Hu, Recent progresses of micro-nanostructured transition metal compound-based electrocatalysts for energy conversion technologies, *Sci. China Mater.*, 2021, **64**, 1–26.
- 19 W. J. Niu, J. Z. He, B. N. Gu, M. C. Liu and Y. L. Chueh, Opportunities and Challenges in Precise Synthesis of Transition Metal Single-Atom Supported by 2D Materials as Catalysts toward Oxygen Reduction Reaction, *Adv. Funct. Mater.*, 2021, **31**, 1–28.
- 20 H. Wang, M. Zhou, P. Choudhury and H. Luo, Perovskite oxides as bifunctional oxygen electrocatalysts for oxygen evolution/reduction reactions – A mini review, *Appl. Mater. Today*, 2019, **16**, 56–71.
- 21 P. Ramakrishnan, H. Im, S. H. Baek and J. I. Sohn, Recent Studies on Bifunctional Perovskite Electrocatalysts in Oxygen Evolution, Oxygen Reduction, and Hydrogen Evolution Reactions under Alkaline Electrolyte, *Isr. J. Chem.*, 2019, **59**, 708–719.
- 22 T. Hyodo, M. Hayashi, N. Miura and N. Yamazoe, Catalytic Activities of Rare-Earth Manganites for Cathodic Reduction of Oxygen in Alkaline Solution, *J. Electrochem. Soc.*, 1996, **143**, L266–L267.
- 23 J. A. M. Van Roosmalen, E. H. P. Cordfunke, R. B. Helmholtz and H. W. Zandbergen, The Defect Chemistry of LaMnO₃ ± δ, *J. Solid State Chem.*, 1994, **110**, 100–105.
- 24 Y. Xue, H. Miao, S. Sun, Q. Wang, S. Li and Z. Liu, La_{1-x}Ag_xMnO₃ electrocatalyst with high catalytic activity for oxygen reduction reaction in aluminium air batteries, *RSC Adv.*, 2017, **7**, 5214–5221.



- 25 Y. Xue, S. Sun, Q. Wang, H. Miao, S. Li and Z. Liu, $\text{La}_{0.7}(\text{Sr}_{0.3-x}\text{Pdx})\text{MnO}_3$ as a highly efficient electrocatalyst for oxygen reduction reaction in aluminum air battery, *Electrochim. Acta*, 2017, **230**, 418–427.
- 26 F. Lu, J. Sui, J. Su, C. Jin, M. Shen and R. Yang, Hollow spherical $\text{La}_{0.8}\text{Sr}_{0.2}\text{MnO}_3$ perovskite oxide with enhanced catalytic activities for the oxygen reduction reaction, *J. Power Sources*, 2014, **271**, 55–59.
- 27 C. Jin, X. Cao, L. Zhang, C. Zhang and R. Yang, Preparation and electrochemical properties of urchin-like $\text{La}_{0.8}\text{Sr}_{0.2}\text{MnO}_3$ perovskite oxide as a bifunctional catalyst for oxygen reduction and oxygen evolution reaction, *J. Power Sources*, 2013, **241**, 225–230.
- 28 S. K. Chandrabanshi, S. Mukhopadhyay and R. Mukherjee, Oxidation of iodide with a mononuclear manganese(IV) complex ion: Mechanistic investigation of autocatalytic behaviour, *Polyhedron*, 2020, **187**, 114664.
- 29 B. Ravel and M. Newville, ATHENA, ARTEMIS, HEPHAESTUS: data analysis for X-ray absorption spectroscopy using IFEFFIT, *J. Synchrotron Radiat.*, 2005, **12**, 537–541.
- 30 S. Angel, F. Schneider, S. Apazeller, W. Kaziur-Cegla, T. C. Schmidt, C. Schulz and H. Wiggers, Spray-flame synthesis of LaMO_3 ($\text{M} = \text{Mn}, \text{Fe}, \text{Co}$) perovskite nanomaterials: Effect of spray droplet size and esterification on particle size distribution, *Proc. Combust. Inst.*, 2021, **38**, 1279–1287.
- 31 J. Suntivich, H. A. Gasteiger, N. Yabuuchi, H. Nakanishi, J. B. Goodenough and Y. Shao-Horn, Design principles for oxygen-reduction activity on perovskite oxide catalysts for fuel cells and metal–air batteries, *Nat. Chem.*, 2011, **3**, 546–550.
- 32 L. Wang, C. Wang, H. Xie, W. Zhan, Y. Guo and Y. Guo, Catalytic combustion of vinyl chloride over Sr doped LaMnO_3 , *Catal. Today*, 2019, **327**, 190–195.
- 33 Y. N. Lee, R. M. Lago, J. L. G. Fierro, V. Cortés, F. Sapiña and E. Martínez, Surface properties and catalytic performance for ethane combustion of $\text{La}_{1-x}\text{K}_x\text{MnO}_{3+\delta}$ perovskites, *Appl. Catal., A*, 2001, **207**, 17–24.
- 34 M. O'Connell, A. K. Norman, C. F. Hüttermann and M. A. Morris, Catalytic oxidation over lanthanum-transition metal perovskite materials, *Catal. Today*, 1999, **47**, 123–132.
- 35 M. Imamura, N. Matsubayashi and H. Shimada, Catalytically active oxygen species in $\text{La}_{1-x}\text{Sr}_x\text{CoO}_{3-\delta}$ studied by XPS and XAFS spectroscopy, *J. Phys. Chem. B*, 2000, **104**, 7348–7353.
- 36 K. Selvakumar, S. M. Senthil Kumar, R. Thangamuthu, K. Ganesan, P. Murugan, P. Rajput, S. N. Jha and D. Bhattacharyya, Physiochemical investigation of shape-designed MnO_2 nanostructures and their influence on oxygen reduction reaction activity in alkaline solution, *J. Phys. Chem. C*, 2015, **119**, 6604–6618.
- 37 A. Paolone, C. Castellano, R. Cantelli, G. Rousse and C. Masquelier, Evidence of a splitting of the Mn–O distance and of a large lattice disorder in the charge-ordered phase of LiMn_2O_4 obtained by EXAFS, *Phys. Rev. B: Condens. Matter Mater. Phys.*, 2003, **68**, 1–5.
- 38 R. Zhou, Y. Zheng, M. Jaroniec and S. Z. Qiao, Determination of the Electron Transfer Number for the Oxygen Reduction Reaction: From Theory to Experiment, *ACS Catal.*, 2016, **6**, 4720–4728.

